Automatic Segmentation of the Wire Frame of Stent Grafts from CT Data*

Almar Klein*[a], J. Adam van der Vliet[b], Luuk J. Oostveen[c],
Yvonne Hoogeveen[c], Leo J. Schultze Kool[c], W. Klaas Jan Renema[c], Cornelis H. Slump[a]

* Corresponding author. e-mail: a.klein@utwente.nl, tel: +31 53 489 2897
[a]Institute of Technical Medicine, University of Twente,
PO Box 217, 7500 AE Enschede, The Netherlands;
[b]Dept. of Surgery, Radboud University Nijmegen Medical Center,
PO Box 9101, 6500 HB Nijmegen, The Netherlands;
[c]Dept. of Radiology, Radboud University Nijmegen Medical Center,
PO Box 9101, 6500 HB Nijmegen, The Netherlands.

January 30, 2012

Abstract

Endovascular aortic replacement (EVAR) is an established technique, which uses stent grafts to treat aortic aneurysms in patients at risk of aneurysm rupture. Late stent graft failure is a serious complication in endovascular repair of aortic aneurysms. Better understanding of the motion characteristics of stent grafts will be beneficial for designing future devices. In addition, analysis of stent graft movement in individual patients in vivo can be valuable for predicting stent graft failure in these patients.

To be able to gather information on stent graft motion in a quick and robust fashion, we propose an automatic method to segment stent grafts from CT data, consisting of three steps: the detection of seed points, finding the connections between these points to produce a graph, and graph processing to obtain the final geometric model in the form of an undirected graph.

Using annotated reference data, the method was optimized and its accuracy was evaluated. The experiments were performed using data containing the AneuRx and Zenith stent grafts. The algorithm is robust for noise and small variations in the used parameter values, does not require much memory according to modern standards, and is fast enough to be used in a clinical setting (65 and 30 seconds for the two stent types, respectively). Further, it is shown that the resulting graphs have a 95% (AneuRx) and 92% (Zenith) correspondence with the annotated data.

The geometric model produced by the algorithm allows incorporation of high level information and material properties. This enables us to study the in vivo motions and forces that act on the frame of the stent. We believe that such studies will provide new insights into the behavior of the stent graft in vivo, enables the detection and prediction of stent failure in individual patients, and can help in designing better stent grafts in the future.

Keywords

stent graft; segmentation; geometric model; AAA; computed tomography

Research highlights

- The proposed algorithm segments the wire frame of stent grafts.
- Comparison with annotated reference data shows a good agreement.
- The resulting geometric model describes the stent in a concise and natural manner.
- We will use this model to study in vivo motions and forces of the stent.

*Appeared in Medical Image analysis, Vol 16, No 1, Januari 2012

1 Introduction

1.1 Clinical context

Endovascular aortic replacement (EVAR) is an established technique, which uses stent grafts to treat aortic aneurysms in patients at risk of aneurysm rupture (Bruin et al., 2010; Investigators, 2010; Zarins et al., 1999). The long-term durability of these stent grafts is affected by the stresses and hemodynamic forces applied to them, and may be reflected by the movements of the stent graft itself during the cardiac cycle. Late stent graft failure is a serious complication in endovascular repair of aortic aneurysms (Cao et al., 2009; Demirci et al., 2009; Jacobs et al., 2003; Li and Kleinstreuer, 2006a; Mattes et al., 2005; Roos et al., 2005), such as the formation of endoleaks (blood flow into the aneurysm sac) that can result in aneurysm expansion and rupture (Li and Kleinstreuer, 2006b; Lu et al., 2008; Stavropoulos and Charagundla, 2007). Better understanding of the motion characteristics of stent grafts will likely be beneficial for designing future devices. In addition, these data can be valuable in predicting stent graft failure in individual patients (Langs et al., 2007, 2011).

Applying ECG-gated CTA (Fuchs et al., 2000) provides three dimensional datasets at different phases of the cardiac cycle. This allows 4D visualization of the scanned object and enables the investigation of its temporal behavior. ECG-gated CT has been used to study the motions of aneurysms (Hazer et al., 2009; Muhs et al., 2006; Wentz et al., 2007) and stent grafts (Langs et al., 2007; Teutelink et al., 2007). In recent work (Klein et al., 2009a) it was found that ECG gating is a suitable technique for studying the expected motions in the stent graft and vessel wall in abdominal aortic aneurysm (AAA).

Most studies on the motion of stent grafts focus on measuring the stent's diameter changes (van Herwaarden et al., 2006) or finding the motion for a sparse set of points on the stent (Langs et al., 2007). A model that enables capturing material properties and high level knowledge about the stent graft would be a valuable tool to gain more insight into the stent's in vivo behavior (Langs et al., 2007). Such a model can also help in performing more reliable (fluid dynamics) simulations, which is important for improving current stent designs (Cebral et al., 2009; Kleinstreuer et al., 2007). To the best of our knowledge such a model has not yet been proposed in literature.

One of the major downsides of CT in general, is the exposure of the patient to ionizing radiation, which can have negative effects on the long term health of the patient (Prokop, 2005; Fazel et al., 2009). The dose should therefore be kept as low as possible. However, this results in higher noise levels and more image artifacts, which can be a problem for automatic image analysis algorithms that often need high quality data to operate. Algorithms that can perform their task on low dose data can therefore contribute to better patient safety.

1.2 Contributions

In this work we take an important step towards evaluating the motion of stent grafts in vivo: the segmentation of the stent graft and its representation using a geometric model.

We propose a geometric model that represents the wire frame of the stent as an undirected graph, with nodes placed at the corners and crossings of the frame, and the edges between the nodes representing the wires (Figure 1). This model represents the topology of the stent's frame in a concise and natural manner.

The main goal of the present work is to present a method to obtain the geometric model of the stent's wire frame from volumetric CT data. The method is fast and robust for high levels of noise, such that it is applicable to CT data obtained with relatively low dose. To evaluate the quality of the produced geometric model, we performed experiments in which the produced model was compared with a reference model annotated by three experts.

1.3 Outlook

The geometric models produced by the proposed algorithm enable future studies on the motion of stent grafts in vivo; the motion field between the cardiac phases (which can be obtained by image registration) capture the motion of the stent and can be used to apply motion to the model. This will give quantitative information about the motion of stent grafts. Subsequently, by incorporating material properties such as stiffness, and by calculating the change of the angle between two edges, the forces present at the stent's frame can be estimated (Figure 1c). Both parameters will add valuable information to the analysis of stent grafts in vivo.

To be useful in future motion analysis, it is of importance that the model precisely represents the topology of the wire frame of the stent graft; if the model contains erroneous or missing nodes or edges, the force calculations can produce invalid results.

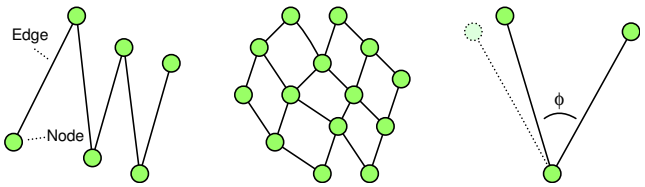

Figure 1: Example graphs that describe a geometric model of the stent's frame. The edges between the nodes represent the physical wire frame of the stent. Nodes are placed at corners (a) and crossings (b), which makes it possible to model different stent types. The (change of) angle ϕ when motion is applied to the model can be used to estimate the force present in the node (c).

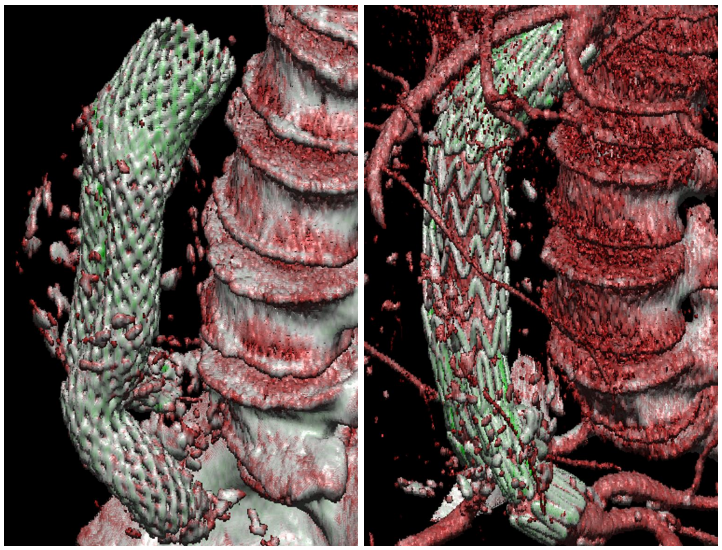

(a) AneuRx (b) Zenith

Figure 2: Illustration of iso-surface renderings from CT data of two different types of stent grafts.

While the proposed method can be applied to non-gated CT data, in the present work ECG-gated data was used because of our intentions to study stent graft motion in the future.

1.4 Previous work

Few results have been published for the segmentation of the wire frame of stent grafts from CT data, despite the need for such a technique to evaluate large 3D datasets. In preliminary work we segmented the wire frame of the stent in 2D slices (Klein et al., 2008). In a recent work by Langs et al. (2011), the stent's frame (in the thoracic aorta) is found using a statistical model. They report that a threshold at 2000 Hounsfield Units is sufficient to obtain a connected set of points belonging to the stent. Unfortunately, our data contains too much noise (compared to the stent's intensities) for such a method. This can be due to differences in the applied dose (which is not not reported in Langs et al. (2011)) or in the material of the stent's frame.

Several studies have been published on the segmentation of blood vessels in 3D, which have similarities with the wires of the frame of the stent (Figure 2) and may therefore be of interest (see Lesage et al. (2009) and Kirbas and Quek (2004) for an overview of vessel segmentation methods). One common method is the two-step approach (Freiman et al., 2009; Kaftan et al., 2009; Manduca et al., 2009; Worz et al., 2009), which first segments the vessel using a vessel measure (Frangi et al., 1998) followed by centerline extraction. Unfortunately, this method is not suitable for our research question because of gaps that can occur in the wire due to artifacts, and the sharp corners of the wire which blood vessels do not posses (Figure 2). Methods that fit a series of spheres or ellipsoids to the vessel (Beck et al., 2009; Zhou et al., 2008), and methods that segment the contour in slices perpendicular to the vessel centerline (Hernandez-Hoyos et al., 2002; Lee et al., 2007) assume a solid vessel with a diameter of several voxels. Due to the small diameter of the stent's wire (1 to 3 voxels) and its

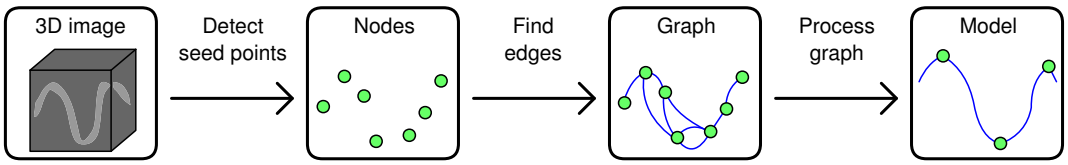

Figure 3: Flowchart illustrating the required processing steps to extract a geometrical model from the CT data.

sharp corners these methods are also not suitable. Region growing methods (Bock et al., 2008) have problems with leaks and gaps and need a second stage to find the geometry from the segmented voxels.

In recent work (Klein et al., 2009b) we have proposed three tracking algorithms to find the optimal path along the wire of the stent, and compared them in an experiment. It was found that the method based on the Minimum Cost Path (MCP) method produced the best results. In the current work, we use the MCP method to segment the stent in a direct manner rather than applying a tracking approach. Additionally, the current work describes the method to create a geometrical model from the results obtained by the MCP method.

1.5 Outline

First the algorithm to calculate the geometric model from the CT data is discussed in three steps in section 2. Next, in section 3, we discuss the experiments that were performed to determine the optimal values for the algorithm's parameters, and the experiments to evaluate the accuracy of the algorithm. Finally, the results are discussed in section 4.

In this work we consider two types of stent grafts which are commonly used in our institution to treat patients with AAA: the AneuRx (Medtronic, Minneapolis, USA) and the Zenith (Cook, Bloomington, USA) stent graft (Figure 2). The proposed method should be general enough to be capable of segmenting the wire frame of both types of stent grafts.

2 Methods

Given are multiple volumetric images $V(\mathbf{x}) \rightarrow \mathbb{R}$ with $\mathbf{x} = (x, y, z)$, acquired from a CT scanner using ECG-gating; each image represents a phase in the cardiac cycle. In a pre-processing step of the proposed segmentation algorithm, n_{phases} volumes are averaged to reduce the noise at the cost of increased motion artifacts. The averaged phases are taken from the end-diastole, which suffers the least from motion artifacts (Desjardins and Kazerooni, 2004). In section 3 the optimal number of phases to average is determined in an experiment.

The proposed method can be divided into three steps, which are illustrated in the flow chart in Figure 3. First, seed points are detected that are likely to be on the wire of the stent, resulting in a set of nodes $\mathbf{p}_i = (x, y, z)$ with $i \in [0 \ldots N-1]$ and N the number of nodes. These nodes represent a graph without edges. In the next step, the edges between the nodes are found using a modified version of the MCP method, resulting for each node $\mathbf{p}_i$ in a set of edges e_{ij}, each connecting it to another node $\mathbf{p}_j$. Finally, the resulting graph is processed by introducing new nodes and removing unwanted nodes and edges. These three steps are discussed in the following subsections.

2.1 Detecting the seed points

A set of seed points is found by searching V for voxels subject to three criteria:

- The voxel intensity must be a local maximum.
- The voxel intensity must be higher than a predefined threshold value v_{seed}.
- The voxel must have a direct neighbor with an intensity also above this threshold value.

Because the frame of the stent has an intensity that is (locally) constant, local maxima—and thus the resulting seed points—are distributed homogeneously along the wire frame of the stent. Since the diameter of the wire of the stent graft is much smaller than the voxels size, the partial volume effect causes the center of wire crossings (in the AneuRx stent graft) to always be a local maximum.

2.2 Connecting the seed points

The seed points are connected using a modified version of the minimum cost path (MCP) algorithm. The MCP method can be used for segmentation of vessels and other structures (e.g. Cohen and Deschamps (2007); Deschamps and Cohen (2000); Fahmi et al. (2008); Gülsün and Tek (2008); Jandt et al. (2009); Quek and Kirbas (2001); Wink et al. (2004)). It is a level set method in which a front is propagated monotonically following a (non-negative) cost function. The advantage of this method is that it can be implemented in a computationally efficient way. It is a form of Dijkstra's algorithm (Dijkstra, 1959) that finds the shortest path in a graph of connected nodes. In the MCP method the nodes are represented by the pixels/voxels, and the edges are implicitly defined by the grid; each node is connected to its direct neighbors.

2.2.1 Theory

Given a set of seed points $P = \{\mathbf{p}_1, \mathbf{p}_2, \ldots, \mathbf{p}_n\}$ (with $\mathbf{p}_i = (x, y, z)$) and the costs in each voxel $C(\mathbf{x}) \rightarrow \mathbb{R}$, the algorithm iteratively calculates the cumulative costs $D(\mathbf{x}) \rightarrow \mathbb{R}$ it takes to travel from the seed points to any other point in the image (Algorithm 1). The minimum cost path from any voxel $\mathbf{x} = (x, y, z)$ to the seed point can be found by backtracking using D.

A major difference with respect to Dijkstra's algorithm is that the costs are defined at the voxels (i.e. nodes) rather than at the edges. Therefore, voxels $\mathbf{n}$ and $\mathbf{m}$ should contribute equally to the transition cost. This fact is sometimes neglected in literature, in which case line 9 in Algorithm 1 is replaced by $d = D(\mathbf{m}) + C(\mathbf{n})$, which resembles the update rule of Dijkstra's algorithm.

By weighting with the Euclidean distance between the voxels, the method corrects for the larger distance for diagonal voxels, and can account for the anisotropicity of the data. In applications where the cost and cumulative cost represent a distance measure, it is advantageous to consider the 8 (2D) or 26 (3D) nearest neighbors rather than only the 4 (2D) or 6 (3D) neighbors; the shape of the front is in that case octagonal rather than square, which results in smaller discretization errors.

A related method is the Fast Marching method (**?**) which replaces line 9 in Algorithm 1 with a formula to solve the Eikonal equation. It therefore remains (more) consistent with the continuous formulation of the problem, which significantly reduces the discretization errors. However, these errors are not significant in our situation since the paths are relatively short and the intensity difference between the wire and the background is relatively large. Additionally, the backtracking algorithm in the resulting cumulative cost map—which is applied relatively often in the proposed method—is considerably more easy and faster for the MCP method.

2.2.2 Cost function

Since the stent is made of metal, it is represented in the data $V(\mathbf{x})$ with relatively high CT-values compared to the soft tissue in the human body. Therefore we define our cost function such that an increase in CT-value results in a decrease in cost:

$$C(\mathbf{x}) = 2^{-V(\mathbf{x})/v_{aff}}, \tag{1}$$

where v_{aff} is a predefined value representing the algorithm's affinity for high intensities. Consider two hypothetical paths, of which one is exactly twice as long as the other but running through voxels of higher intensities. The above formula implies that the longer path is preferred if the intensities over the path are at least v_{aff} Hounsfield Units higher. This increased affinity for high values over a shorter path prevents the algorithm from cutting (sharp) corners.

2.2.3 Implementation

The MCP method can easily be modified to make it more suitable for a specific problem. For example, in Klein et al. (2009b) the algorithm executes until a certain distance from the seed point is reached, and in Cohen and Deschamps (2007) the traveled distance of the front compared to the largest travelled distance is used as a measure to freeze the front and thus prevent leaking outside the vessel.

In the present work the MCP algorithm is modified (Algorithm 2) such that the fronts evolve from all the seed points $\mathbf{p}_i$ found in the seed point detection step (section 2.1). Connections between the nodes are detected when two fronts collide. As the fronts propagate, two maps are maintained (both maps are initialized with all values to -1). The first is the backtrack map B that specifies for each point what the previous point was. The second is the identification map I, a Voronoi diagram (Aurenhammer et al., 2000) that specifies for each point $\mathbf{x}$

Algorithm 1 Pseudo code for the normal Minimum Cost Path method.

```
01 function MCP(C):
02   init cumulative cost map D(x) = ∞ ∀x
03   init D(p_i) = 0 for all seed points
04   insert the seed points in list L
05   while not isempty(L):
06     take voxel m from L with minimum D
07     for n in neighborsOf(m):
08       δ = euclideanDist(n,m)
09       d = D(m) + 1/2 · δ · (C(n) + C(m))
10       if d < D(n):
11         D(n) = d
12         if n not in L:
13           insert n in L
14   return D
```

Algorithm 2 Pseudo code for the proposed (modified) version of the Minimum Cost Path method.

```
01 function MCP_connect_seed_points(C):
02   init D(x) = ∞, I(x) = −1, B(x) = −1 ∀x
03   init D(p_i) = 0 for all seed points p_i
04   init B(p_i) = i for all seed points p_i
05   init I(p_i) = i for all seed points p_i
06   insert the seed points in list L
07   while not isempty(L):
08     take voxel m from L with minimum D
09     for n in neighborsOf(m):
10       if I(n) ≠ −1 and I(n) ≠ I(m):
11         makeEdge(n,m)
12       δ = EuclideanDist(n,m)
13       d = D(m) + 1/2 · δ · (C(n) + C(m))
14       if d < D(n):
15         D(n) = d
16         B(n) = m
17         I(n) = I(m)
18         if n not in L:
19           insert n in L
20   return edges
```

from which seed point it originates: $I(\mathbf{x}) \rightarrow i$, maps point $\mathbf{x}$ to seed point $\mathbf{p}_i$. Consequently, the collision of two fronts can be detected by testing $I(\mathbf{m}) \neq I(\mathbf{n})$ and $I(\mathbf{n}) \neq -1$ (line 10 in Algorithm 2). If this test is positive, an edge e_{ij} between nodes $\mathbf{p}_i$ and $\mathbf{p}_j$ is created (with $i = I(\mathbf{n})$ and $j = I(\mathbf{m})$), and the path between $\mathbf{p}_i$ and $\mathbf{p}_j$ is found by backtracing the route using B (Figure 4b). Since it is possible that another (lower cost) path between i and j is found later (Figure 4c), the above check should be performed at each iteration and for each neighbor. Figure 4d shows how the front originating from one seed point partly replaces another front, thereby changing the identification map I and the backtrack map B. This illustrates that the paths need to be traced at the moment an edge is found.

As a stop criterion the value of $D(\mathbf{m})$ is compared to a predefined threshold d_{max}. If the threshold is reached, the cumulative cost is at such a level that we can assume all significant edges have been found.

2.3 Graph processing

The result of the MCP algorithm is a graph consisting of nodes (the seed points) connected by edges. Each edge is associated with a path $P_{ij} = [\mathbf{p}_i, \ldots, \mathbf{p}_j]$ of voxels connecting one node to another. Although the paths themselves are optimal (in terms of the cost C), many of these edges are false edges, and must be removed. For this purpose, two scalar values are associated with each edge. The first is α_{ij}, the maximum cumulative cost $D(\mathbf{x})$ on the path. It represents the *weakness* (i.e. inverse strength) of the edge. This value is used to establish the order of the edges; a stronger connection (lower α) is preferred over a weaker one. The second scalar value is β_{ij}, the minimum intensity (the CT-value in Hounsfield Units) on the path. Due to the definition of CT-values

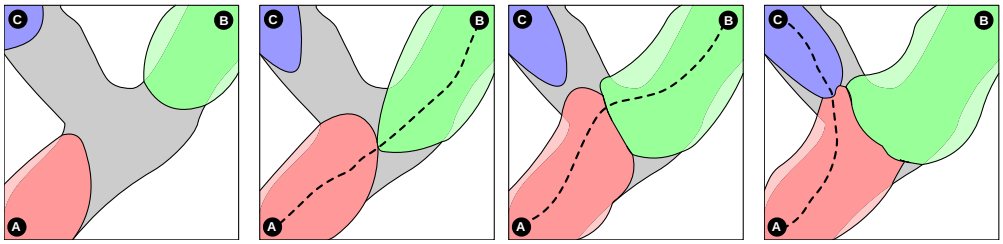

Figure 4: Illustration of three meeting fronts. The black circular shapes indicate seed points A, B and C. In (a) the fronts do not yet meet. In (b) front A meets front B, and the path is traced. A few iterations later, in (c) a better path (lower D) is found between A and B. The path is traced again and updated. In (d) a third front meets with the first, connection seed points A and C.

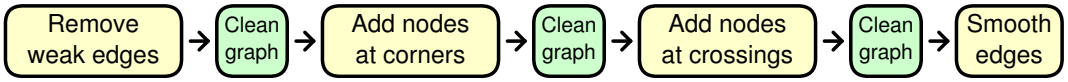

Figure 5: Flow chart illustrating the process of graph processing.

(-1000 representing air and 0 representing water) this value has a physical meaning and represents the *quality* of the edge; it is used to determine whether an edge should be removed or not. The processing of the graph occurs in multiple different passes which are illustrated in Figure 5 and described below.

1. **Removing weak edges.** Weak edges are removed based on the expected number of edges for each node n_e, which is two for the Zenith and four for the AneuRx stent graft. The algorithm iterates over all nodes $\mathbf{p}_i$, and evaluates their edges. If a node has more than n_e edges, the weakest surplus edges are selected (using α_{ij}) and considered for removal: the edge e_{ij} is removed if β_{ij} is smaller than the predefined threshold $v_{quality}$, and if the same criteria are also met when considering the edge from the node at the other end ($\mathbf{p}_j$). If $\beta_{ij} > v_{quality}$ there is enough evidence to assume the path P_{ij} corresponds to a wire and the edge e_{ij} is considered valid (Figure 6a).

2. **Clean-up.** Next, redundant edges are removed: all connections s_{ij} are considered in the order of decreasing α_{ij}, starting with the weakest edge. An edge is found redundant if there is a path of one or two stronger (i.e. lower α) edges that connect the same nodes. Next, each cluster (i.e. group of interconnected nodes that is not connected to any other nodes) is removed if it consist of less than $n_{cluster}$ nodes, and each tail (i.e. string of nodes) is trimmed if it consists of less than n_{tail} nodes (Figure 6b).

3. **Adding nodes at corners.** The third pass starts with removing nodes from the graph that have exactly two edges. The two edges are combined to form a new edge. Next, all edges are evaluated and new nodes are inserted at the corners of the wire by searching for points on the path P_{ij} that have maximum curvature (Figure 6c): for each point $\mathbf{x}$ on the path, two vectors are calculated, which each span five positions on the path (corresponding to maximal 5 mm, which is less than the length of the wires). The angle ϕ between the two vectors is calculated (Figure 7), and the resulting angle values for all the points in the edge are smoothed with a Gaussian filter (with a standard deviation of 3 voxels) to account for the discretization. By detecting local minima in the resulting list of angles, the point of maximum curvature can be calculated.

4. Repeat pass 2. Since the graph has changed, new edges can now be marked redundant. These should be removed before proceeding to the next pass. Furthermore, pass 5 gets rid of many nodes in invalid clusters, which therefore are now eligible for removal.

5. **Adding nodes at crossings.** By tracing the paths of two edges from the same node, the algorithm determines whether the paths are partly the same. In these cases a new node is inserted at the point where the paths diverge, and the overlapping parts of the paths are replaced by a single edge (Figure 6e) (Cohen and Deschamps, 2007). This pass is not applied if $n_e = 4$, because in that case the nodes are already correctly positioned at the crossings and this pass would only introduce false crossings.

6. Repeat pass 2. Since the graph has changed, new edges can now be marked redundant (Figure 6f).

7. **Smoothing.** Finally, the paths are smoothed using a moving average filter (with a range of three voxels).

3 Experiments

3.1 Materials

ECG-gated CT data was obtained for 10 different patients (4 with AneuRx, 6 with Zenith) using a Siemens Somatom 64-slice CT scanner (Siemens Medical Solutions, Erlangen, Germany). A rotation time of 0.37 s, a pitch of 0.34, and $2 \times 32 \times 0.6$ mm^2 collimation were used. The effective tube current (per rotation) time product was 180 mAs and the tube voltage was 120 kVp. Each volume was reconstructed using the B36f reconstruction filter and resulted in approximately 300 slices of 512×512 voxels. The slices (with a thickness of 2 mm) were spaced 1 mm apart, and the resolution in the *xy* plane was approximately 0.5 mm. Retrospective gating was applied to obtain 10 (equal distant) cardiac phases. The resulting data were manually cropped to $256 \times 256 \times 256$ voxels to reduce the memory requirements.

For the purpose of creating a reference graph, two dimensional images of unfolded pieces of stent were obtained via radial raycasting. Virtual cylinders were manually aligned with the stent's centerline, and given a diameter slightly larger than that of the stent. Rays were projected (using maximum intensity projection) from the axis onto the face of the cylinder to obtain an unfolded image of the stent (Figure 8a). Since a bifurcation cannot be unfolded in this manner, only tubular sections without bifurcations were used. This resulted in 18 unfolded stent images: 6 of the AneuRx stent graft and 12 of the Zenith stent graft. In total there were approximately 700 edges for each stent type.

An annotation tool was developed which could be used to annotate a graph in the 2D image of the unfolded stent. Using the mouse, nodes could be created, repositioned and removed, and edges between the nodes could be defined. The annotator could initialize the graph with the (un-tuned) algorithm to alleviate the required work for the annotator in regions which can be considered "easy".

Three trained observers (an experienced radiologist, an experienced vascular surgeon and a computer scientist) annotated the stent's frame using the annotation tool. Because the (x,y,z) location in the original volume was known for each pixel in the unfolded images, a three dimensional graph could be obtained from the expert's 2D annotations (Figure 8b), which served as a reference to evaluate the proposed algorithm.

3.2 Comparison Method

To compare the geometric model produced by the algorithm with the annotated reference, a method to compare two graphs is required. In graph theory the *edit distance* (Bunke, 1998) is a common method to compare two graphs. The method considers the list of operations on one graph to transform it into the other. A final distance measure is obtained by adding the costs for each edit operation. Since for the geometric model the edges represent the physical wires, while the nodes are only a way to connect these, we use a cost of 1 to add or remove an edge, and a cost of 0 to add or remove a node. Consequently, the edit distance becomes $N_{miss} + N_{wrong}$, representing the number of false negatives plus the number of false positives. To produce a score expressed as a percentage, we apply the Dice Similarity Coefficient (DSC) (Crum et al., 2006):

$$DSC = \frac{2 \cdot N_{match}}{(N_{match} + N_{miss}) + (N_{match} + N_{wrong})} \cdot 100\% \tag{2}$$

where N_{match} represents the number of true positives.

3.3 Results

Multiple experiments were performed using the annotated reference data. The reference data was divided in a training set containing 6 stent pieces (400 edges in total) obtained from 6 different patients, and a test set containing 12 stent pieces (946 edges in total) obtained from 8 different patients. The sets were divided such that in each set the amount of edges for each stent type is approximately the same. The training set was used for parameter tuning and the test set for measuring the accuracy of the algorithm. The experiments and their results are described in the next paragraphs.

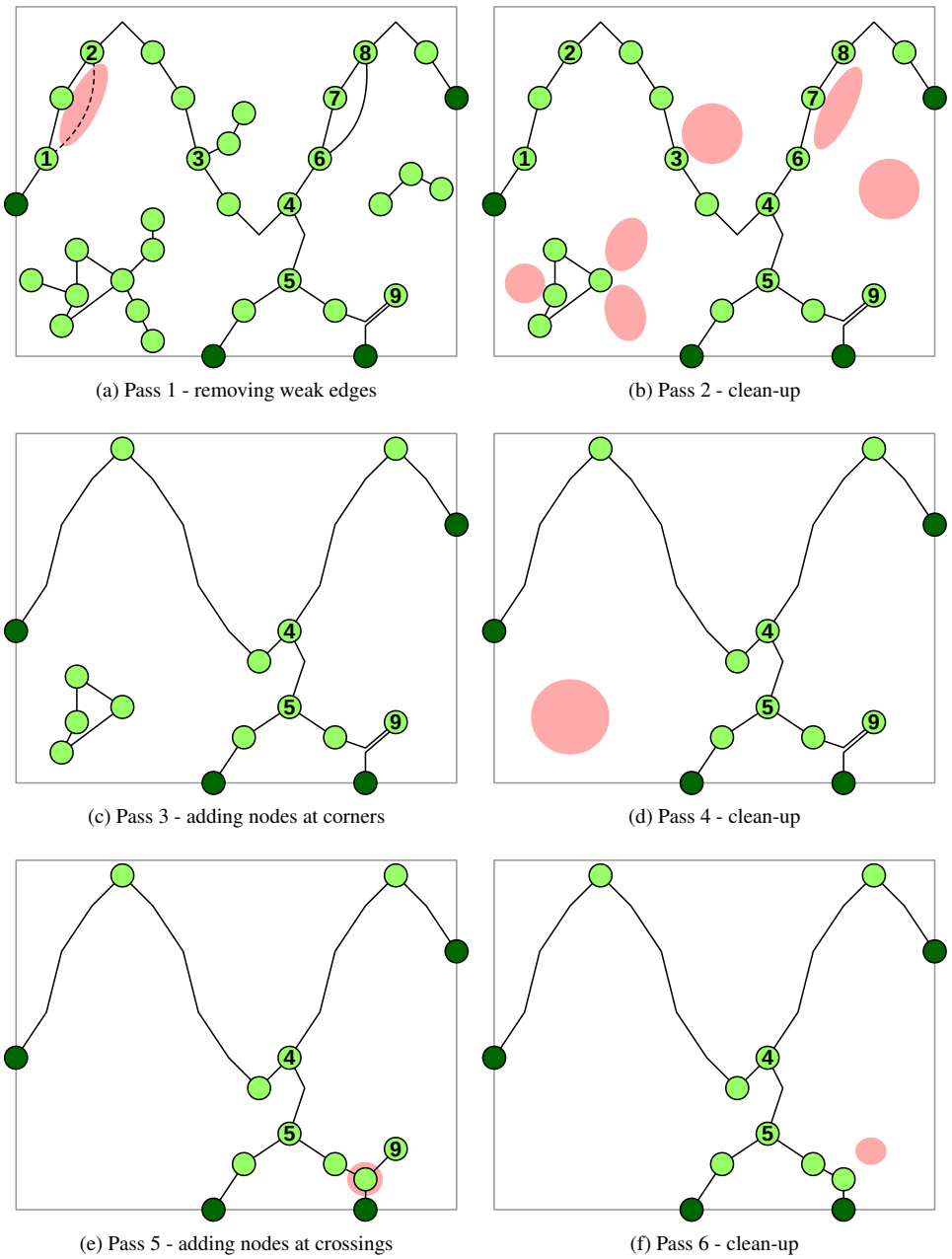

(a) Pass 1 - removing weak edges

(b) Pass 2 - clean-up

(c) Pass 3 - adding nodes at corners

(d) Pass 4 - clean-up

(e) Pass 5 - adding nodes at crossings

(f) Pass 6 - clean-up

Figure 6: Illustration of an example of the different steps in the graph processing. For the sake of the example, the dark nodes at the image boundaries are fixed. Changes are highlighted with red ellipsoids. In (a) the weak ($\beta < v_{quality}$) edge e_{12} is removed because it is found not-expected by both end-nodes. Edge e_{68} is also not expected, but its β is high enough to support evidence of a wire, and the edge is thus not (yet) removed. In (b) e_{68} is removed because it is redundant and e_{67} and e_{78} are apparently stronger. Further the tail at node 3 is removed, as well as a few tails in the bottom-left cluster. The bottom-right cluster is removed because it is too small. In (c) new nodes are placed at corners, and nodes with only two edges are “dissolved". In (d) the bottom-left cluster is removed. In (e) a node is placed at a crossing. In (f) node 9 is removed because it is now on a tail.

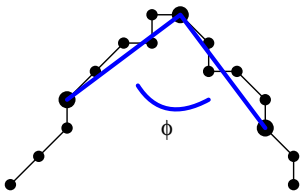

Figure 7: Illustration of how the path's curvature is calculated to be able to insert nodes where the curvature is maximal. The black dots represent voxel positions. The algorithm selects the voxel for which the angle ϕ is the smallest.

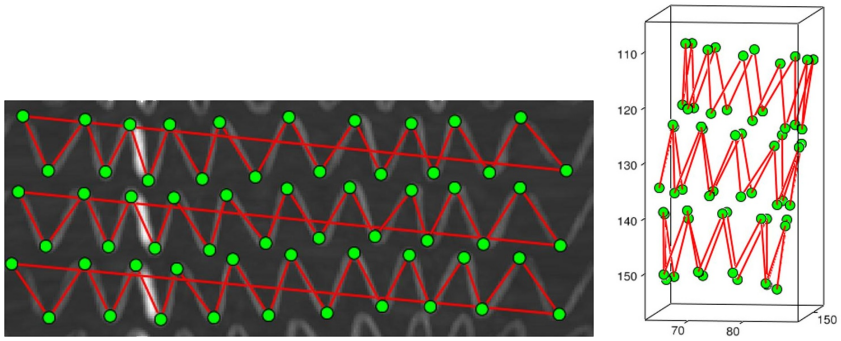

(a) 2D image and annotations (b) Reference graph

Figure 8: Illustration of an example image used for the manual annotations (a), obtained using radial raycasting, and the resulting 3D reference graph (b).

3.3.1 Parameter tuning

To choose suitable values for the parameters of the algorithm and to study the algorithm's sensitivity to the chosen parameter values, tuning experiments were performed on the training set. To tune each parameter (n_{phases}, v_{seed}, d_{max}, v_{aff} and $v_{quality}$), the algorithm was applied multiple times using a range of different values for the parameter. Accuracy plots were generated by comparing the resulting models against the annotated reference data, resulting in one plot per annotator. The resulting accuracy plots are shown in Figure 9. The plots show the optimal value for each parameter, and also give an idea of how sensitive the algorithm is for the parameter value. The parameters (and their found optimal values) are listed in Table 1. Although the removal of tails and small clusters has a positive effect on the resulting geometric model, this cannot be measured in the experiments; because the nodes/edges of tails and erroneous clusters are in general not inside the cylinder that is compared with the reference data, removing these edges has no effect on the accuracy measure.

3.3.2 Accuracy

An experiment to evaluate the accuracy of the algorithm was performed with the test set. Using the optimal parameter values found in the tuning experiments, the algorithm's results were compared with the results of the three annotators. The resulting values for N_{match},N_{wrong} and N_{miss} are given in Table 2, and the matching scores are illustrated in Figure 10a. It can be seen that the accuracy is approximately 95% and 92% for the AneuRx and Zenith respectively. In order to assess the quality of the used reference data, the graphs produced by the annotators were also compared with each-other (Figure 10b).

Figure 11 and Figure 12 give an impression of the different steps of the algorithm and provide a way to visually assess the quality of the algorithm for the AneuRx and Zenith stent graft, respectively. In Figure 13 and Figure 14 surface rendered images of the geometric models of both stent types is shown. [1] For the purpose of visualization, clusters of edges not attached to the stent were manually removed; because the topology of the graph is known, clusters of interconnected nodes are easily identified and can be removed using an interactive process with just a few mouse clicks.

[1] Interactive flash movies of two examples are available at: http://www.sas.el.utwente.nl/home/almar/stents.html

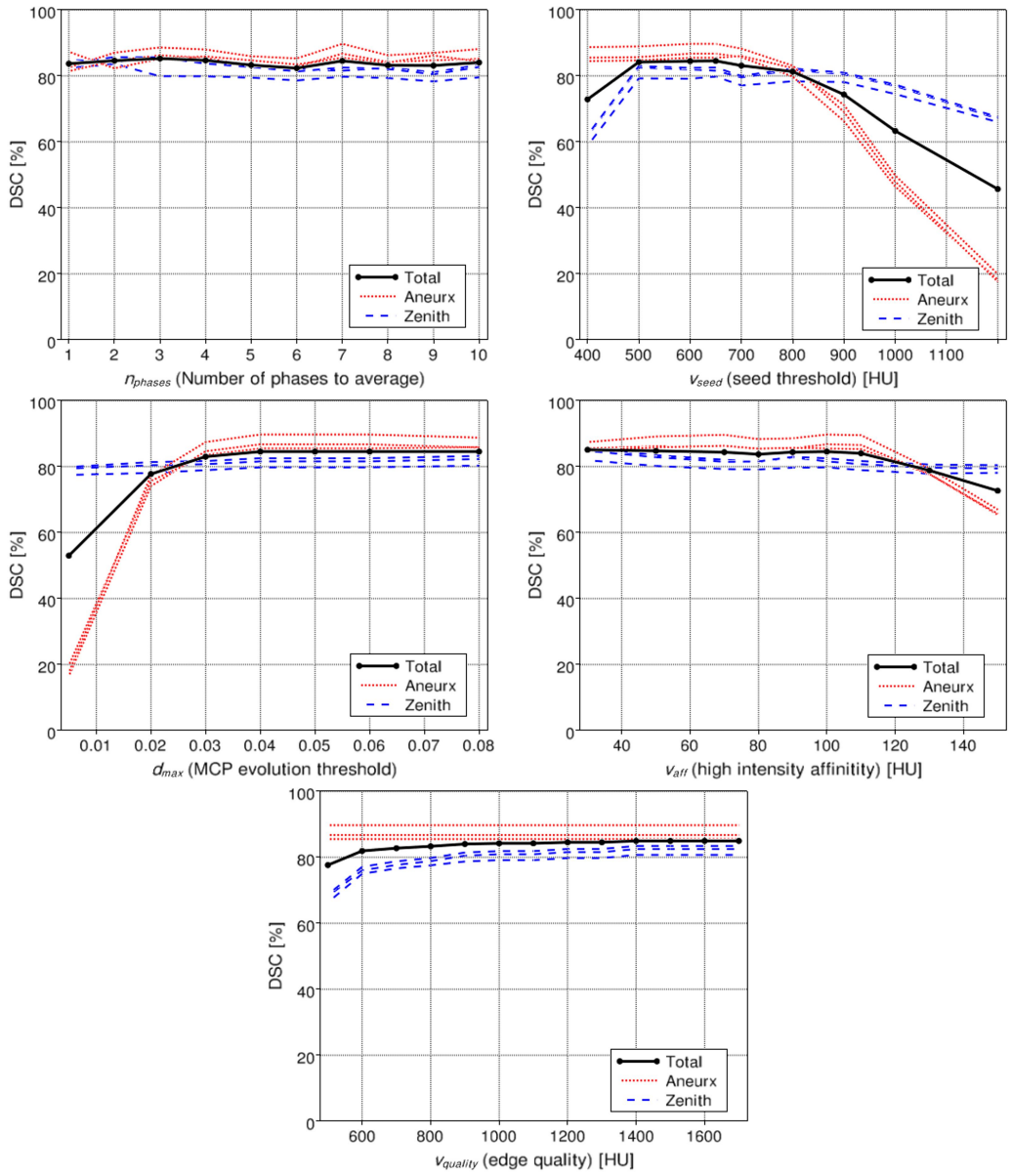

Figure 9: Results for the parameter tuning experiments. Shown are three lines (corresponding to the three annotators) for each type of stent graft, and a thick line indicating the total accuracy.

Parameter	Optimal value	Description
n_{phases}	7	Number of phases to average
v_{seed}	650	Threshold to detect seed points
d_{max}	0.06	MCP evolution threshold
v_{aff}	100	High intensity affinity
$v_{quality}$	1200	Threshold for edge quality
$n_{cluster}$	8	Minimum cluster size
n_{tail}	3	Maximum tail length

Table 1: List of the algorithm's parameters and the resulting optimal values.

Stent type	Annotator	N_{match}	N_{wrong}	N_{miss}	DSC
AneuRx	1	448	16	19	96.2%
	2	448	16	26	95.5%
	3	442	22	19	95.6%
Zenith	1	470	53	21	92.7%
	2	466	57	27	91.7%
	3	470	53	23	92.5%

Table 2: List of the number of true positives, false positives, false negatives and the resulting scores in the accuracy experiment.

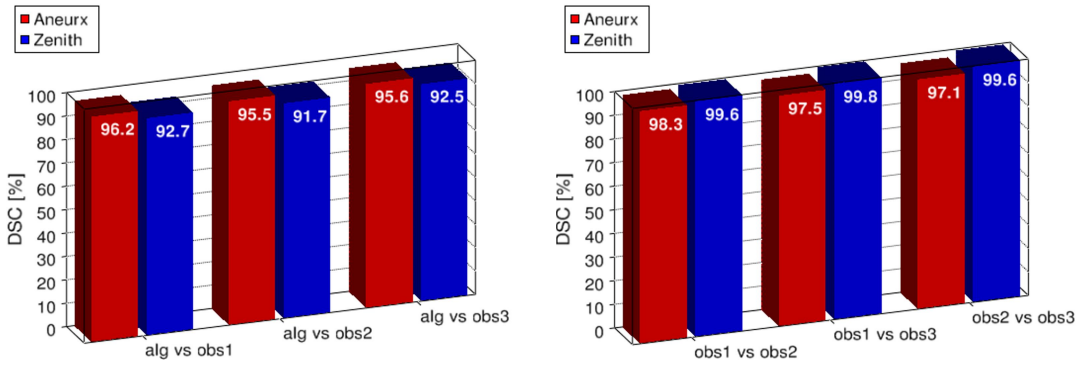

(a) (b)

Figure 10: Illustration of the accuracy of the proposed algorithm (a) and the inter-observer agreement of the annotators (b), measured using the 12 stent pieces from the test set. (“alg" stands for the proposed algorithm, “obs" stands for observer.)

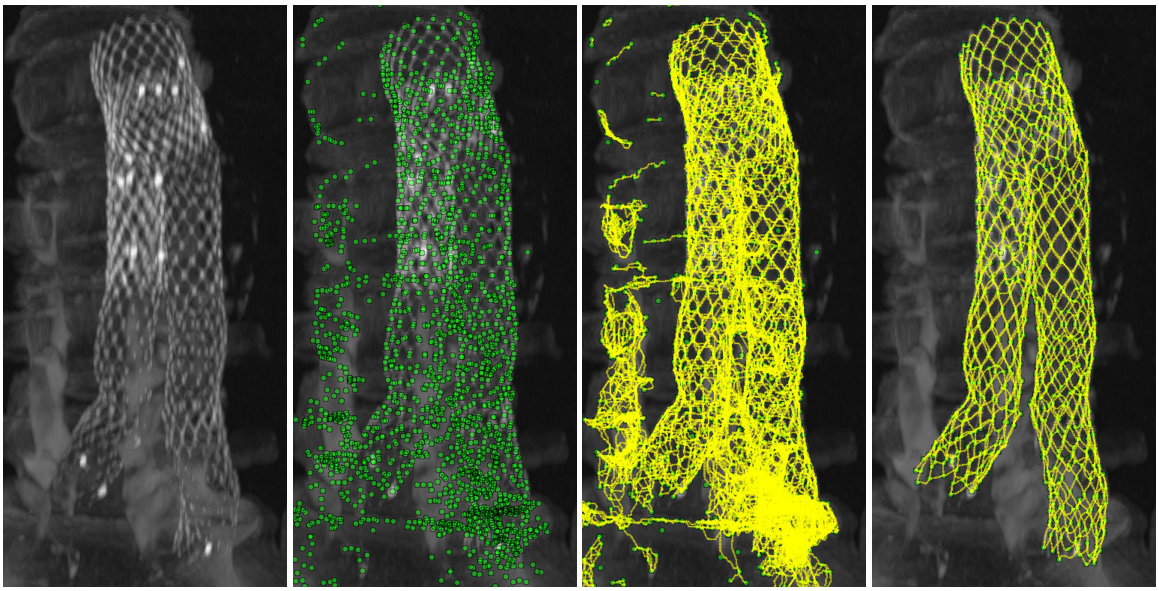

(a) MIP of the CT data (b) 2873 seed points (c) 9630 initial edges (d) 1496 final edges

Figure 11: Illustration of the different algorithm steps for an AneuRx stent graft. Shown are a Maximum Intensity Projection (MIP) of the original data (a), the detected seed points (b), the found edges (c), the result after processing the graph (d).

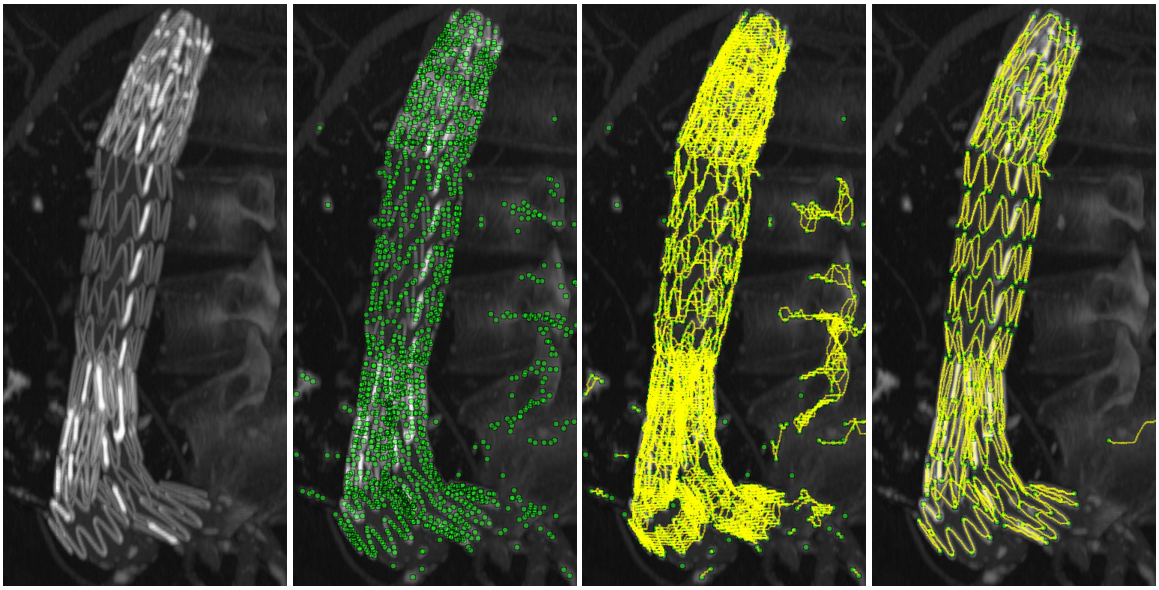

(a) MIP of the CT data (b) 1732 seed points (c) 4963 initial edges (d) 531 final edges

Figure 12: Illustration of the different algorithm steps for a Zenith stent graft. Shown are a Maximum Intensity Projection (MIP) of the original data (a), the detected seed points (b), the found edges (c), the result after processing the graph (d).

4 Discussion

4.1 Parameters

From Figure 9 it can be seen that the plots for most parameters are relatively smooth, which implies that small variations in the parameter values do not affect the accuracy of the algorithm. This means that finding the (global) optimal parameter values is relatively easy, as there are no local maxima and the parameters have little effect on each-other. Additionally, this suggests that the algorithm performs consistently on different data using the same parameter values. However, the optimal parameter values can differ if a different scanner type or different acquisition settings are used. All parameters—except for d_{max}—have a direct relation to a physical quantity and are therefore relatively easy to choose.

The plot for n_{phases} (Figure 9) shows that this parameter has little effect on the accuracy of the algorithm. This suggests that the algorithm is relatively robust for noise. There is a slight decrease after $n_{phases} = 3$, which can probably be attributed by the increase in motion artifacts. Further, the plot shows a small peak at $n_{phases} = 7$. Whether this peak is significant remains uncertain, but it can be explained as follows. The pressure present in the abdominal aorta first rises quickly after which it slowly declines (Hazer et al., 2009; Li and Kleinstreuer, 2006a; Swillens et al., 2008). The phases to average are selected primarily from the diastolic phase. As more phases are selected for averaging, more phases are included that are not in the diastolic phase, and the increased motion artifacts will negate the positive effect of the reduced noise. The peak at the seventh phase can be explained by the fact that the seventh included phase is usually at the maximum of the pressure pulse, where the amount of motion is low, and thus causes a relatively large accuracy increase. Naturally, when a different number of phases are reconstructed, the optimal value of n_{phases} will also change. The relative flatness of this plot is an indication that the algorithm is relatively invariant to noise; the algorithm performs well even when applied to a single phase.

The plot for v_{seed} illustrates a clear maximum accuracy around 650 HU (Hounsfield units). While the materials of which stents are made (stainless steel and nitinol) are usually expressed in much larger CT-values, the partial volume effect causes the parts of the stent where the wire is thin to be represented by CT-values around 650 HU. The accuracy for the AneuRx decays faster because its contrast (in the CT data) is lower than for the Zenith stent graft. This difference can be explained by the difference in material or wire diameter. If the value of v_{seed} is chosen too high, too few seed points are detected in order to segment the stent completely. If the value is chosen too low, many false seed points are introduced that cannot be cleaned up by the graph processing algorithm, particularly when contrast fluid was applied during scanning.

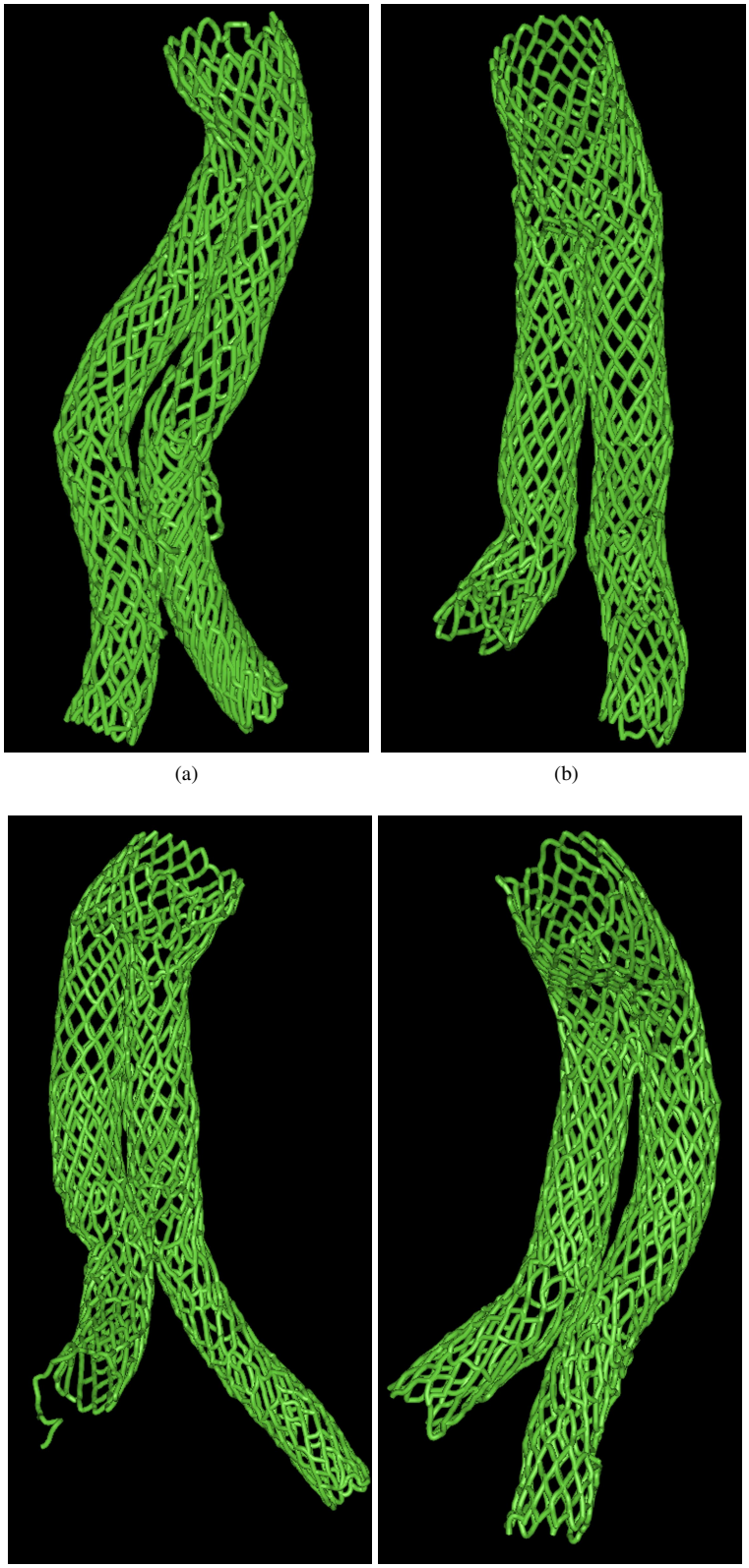

(a) (b)

(c) (d)

Figure 13: Illustration of lit surface renders of the resulting models for the 4 datasets containing the AneuRx stent.

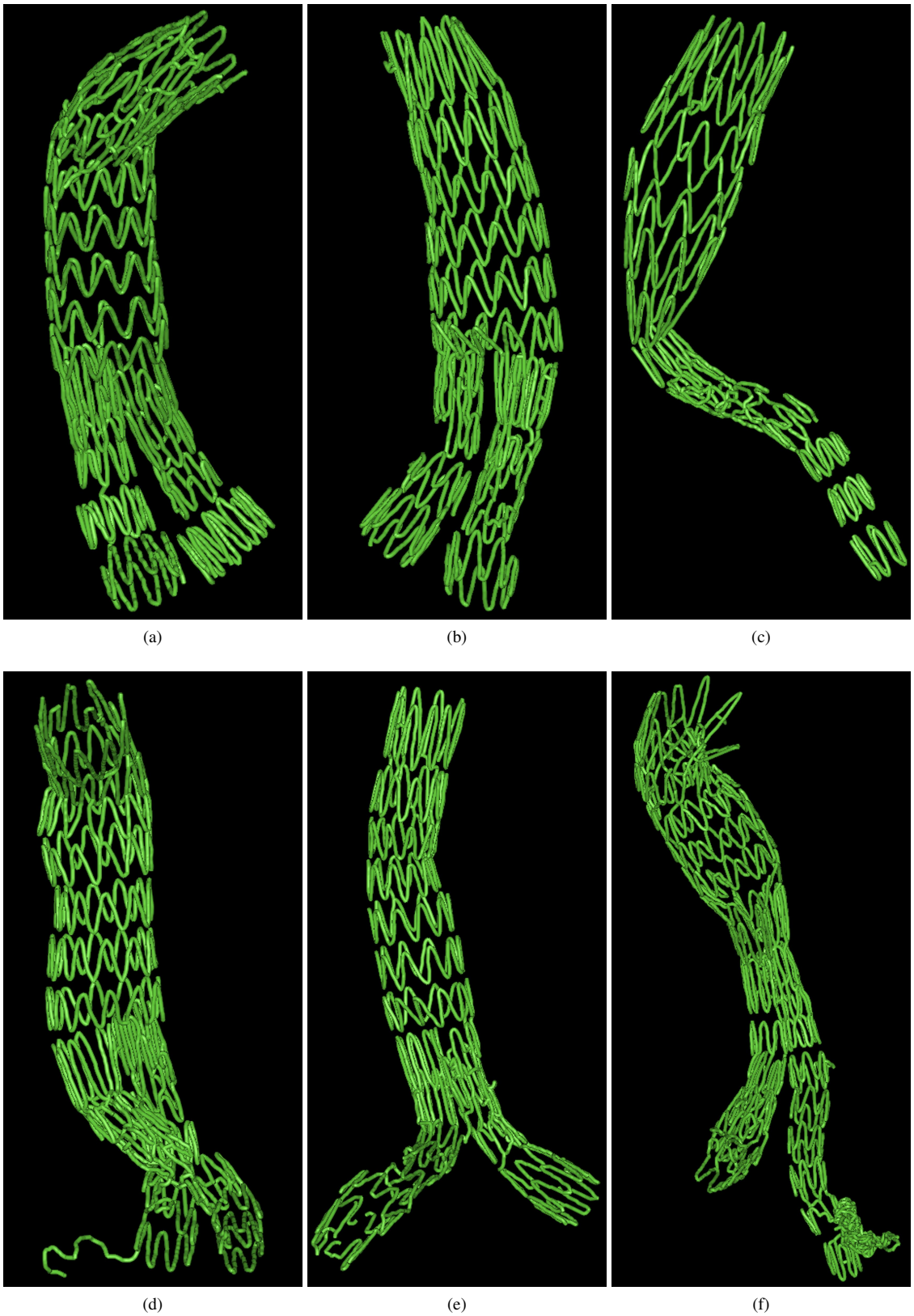

(a) (b) (c)

(d) (e) (f)

Figure 14: Illustration of lit surface renders of the resulting models for the 6 datasets containing the Zenith stent.

The plot for the MCP evolution threshold d_{max} shows the minimal value to use in order not to miss any connections between nodes. While higher values will result in more edges being produced, these are successfully cleaned up by the graph processing algorithm. The plot for the high intensity affinity parameter v_{aff} shows a broad optimum around 100 HU.

The plot for $v_{quality}$ illustrates that this parameter has no effect for the AneuRx stent graft. This suggests that there are usually no extra edges found between nodes. Although the plot suggests that (for the Zenith stent graft) there is no maximum for this parameter value, we chose a value of 1200; the situations in which this parameter is applied (when there are more genuine edges than expected) are relatively rare and are probably not represented sufficiently in the training data. Fortunately, the value can be chosen by considering what it physically represents; an edge with a minimum CT-value of 1200 can only represent bone or a metallic structure. The plot does show that using values lower than 1200 HU results in erroneous edges.

The values of $n_{cluster}$ and n_{tail} could not be chosen based on experimental data (see section 3.3.1), and their values might therefore not be optimal. Visual inspection of the results showed that most tails are successfully removed, but some invalid clusters remain, specifically on the spinal cord (which were removed interactively). Although increasing the value of $n_{cluster}$ might remove these false clusters of nodes, this will also result in parts of the stent being removed (particularly for the Zenith stent graft, for which the graph consists of several non-connected clusters).

In the brief discussion on the algorithm to calculate the curvature on the path P_{ij}, two parameter values were mentioned. These were not tested in the experiments because it was found that the corners are placed in the correct location even when the parameters were varied significantly.

4.2 Accuracy

Figure 10a show that the correspondence of the algorithm with the experienced human annotators is 95% and 92% for the AneuRx and Zenith, respectively. This is currently (to the best of our knowledge) the only published algorithm to segment stent grafts is such a precise way. The fact that the accuracy is slightly lower for the Zenith can be explained by the occasional sharp corners in its wire frame, which are sometimes cut in the MCP method.

Figure 10b shows that the consensus between the different annotators is high. This means that the process of annotating provides consistent reference data and suggests that the reference data is a good approximation of the real topology of the stent. In the future the reference data can be used to perform similar experiments to compare different algorithms that perform the same task.

From Figure 13 and Figure 14 it can be verified that the overall accuracy is good, but some errors are clearly visible. Most errors are located at "difficult situations" such as the parts where the wire frame has relatively sharp corners (Zenith), small mesh size (AneuRx), or bifurcations (AneuRx and Zenith). Further it can be seen that for the AneuRx the frame contains holes, and that nearby structures are sometimes attached to the stent (such as the coil in Figure 14f).

Figure 13 and Figure 14 show that there is still room for improvement. We expect to gain the most by improving the graph processing, for example by more explicitly incorporating information about the known topology of the stent. Nevertheless, we believe that the current results are good enough to enable studying the motion of stent grafts in vivo. However, it should be noted that small errors in the topology of the found model can lead to significant errors when calculating the forces present in the stent. The extent to which the errors affect such calculations should be investigated.

Currently the algorithm requires approximately 65 seconds for the AneuRx and 30 second for the Zenith on a Pentium 4 with 2.4 GHz (using a single thread). This difference can be explained by the different number of edges between the stent types.

4.3 Limitations

In this study we focused on two different stent types—the AneuRx and Zenith—which are made of nitinol (a nickel titanium alloy) and stainless steel, respectively. We expect that the proposed algorithm can be used to segment other stent types as well, provided that the contrast is high enough. This should be the case if such a device is made of a similar material and has the same (or larger) wire diameter. In initial tests (not shown in this work) we have seen positive results for the Talent stent graft (Medtronic, Minneapolis, USA), while the Excluder stent graft (Gore, Flagstaff, USA) seemed too ill-defined in the resulting CT data when scanned with our scanner settings. More research is needed to determine the cause for these differences.

While the optimal parameter values are the same for both stent types under consideration (except for the expected number of edges per node), this is not necessarily true for other stent types.

The annotated reference data does not contains parts of the stent with bifurcations. These are hard to annotate for three reasons: firstly, a bifurcation cannot be unfolded in the way as proposed in this work. Secondly, the topology of the frame can be relatively complex in these regions. Lastly, such regions can contain wires that touch each-other, which are difficult to distinguish from wires that are physically attached. Since the algorithm does not suffer from the first two limitations, we can expect the algorithm to produce accurate results in these regions. This can, however, not be verified with the presented experimental method.

4.4 Implementation details

Most of the algorithm was implemented in the Python programming language[2]. A time-critical part of the algorithm is the list L that stores the voxels of the "front" in the MCP method (Algorithm 1). Because at each iteration the voxel with the minimum D must be selected, usually some form of a binary heap is employed (Deschamps and Cohen, 2000), which enables obtaining the minimum value in $O(log2(N))$. For increased speed, the detection of seed points, the binary heap, and a large part of the MCP method were implemented in Cython (Seljebotn, 2009), a dialect of the Python programming language that is compiled to the C language.

The memory requirements of the algorithm depend mostly on the MCP method. Considering a dataset of $512 \times 512 \times 512$ voxels, the memory requirements can be shown to be 2944 MB to store the volumetric maps required by the MCP method. By cropping the data and selecting the region containing the stent, the data could in our case be reduced to $256 \times 256 \times 256$ voxels, implying a memory requirement of just 368 MB. The latter requirement should not be a problem even for older (32 bit) personal computers.

Accuracy and speed improvements may be achieved by applying a method that detects the seed points in a more reliable way, while reducing the amount of seed points found on bone. Further speed improvements may be realized by using a different criterion to stop the evolution of the MCP algorithm, and by optimizing the graph processing algorithms. Nevertheless, we believe that the algorithm in its current form is fast enough to be used in the clinic.

5 Conclusions

We propose a method to segment stent grafts from CT data, consisting of three steps: the detection of seed points, finding the connections between these points to produce a graph, and graph processing to obtain the final geometric model. Using annotated reference data, the method was optimized and its accuracy evaluated. It was found that the algorithm performs good for both types of stent grafts under consideration and is robust for noise and small variations in the used parameter values. Additionally, the algorithm does not consume much memory for modern standards and is fast enough to be used in a clinical setting.

The proposed algorithm produces an accurate geometric model of the stent in the form of an undirected graph. This model allows incorporation of high level information and material properties. We can now use this model to study the in vivo motions and forces that act on the frame of the stent. We believe that such studies will provide new insights in the behavior of the stent in vivo, enables the detection and prediction of stent failure, and by better understanding the reasons for stent failure can play a role in designing better stent grafts in the future.

Acknowledgment

The authors wish to thank Zachary Pincus from Yale University for the fruitful discussions on the MCP method and its implementation in Cython.

Vitae

Almar Klein received his master in electrical engineering from the University of Twente, the Netherlands, in 2006. He undertook an internship at Philips Applied Technologies, performing research on the SIFT algorithm. During his master thesis he worked on (elastic) image registration of photo's of diabetic feet. In 2007, he commenced his PhD research at the University of Twente on the movement of stent grafts in the abdominal aorta.

[2] http://www.python.org

Daan van der Vliet is professor of Surgery at the Radboud University Nijmegen Medical Centre in the Netherlands, where he chairs the Division of Vascular and Transplant Surgery. He went to medical school in Groningen and received his surgical training at the University Hospital in Maastricht. He wrote his doctoral thesis on organ procurement for transplantation. After a surgical research fellowship at the University of Minnesota in Minneapolis, MN, he undertook a transplant fellowship at the Erasmus University Rotterdam Medical Centre. He served on the boards of several professional societies and is author of more than 150 scientific publications.

After studying physics, Luuk Oostveen worked at the Dutch Expert and Training Centre for Breast Cancer Screening for eight years. His main tasks were quality control of the screening units and research into new developments in mammography. For the past four years he is a member of the Medical Physics team at the department of radiology in the Radboud University Nijmegen Medical Centre, where he is involved in several research projects.

Yvonne L. Hoogeveen attained a BSc from the University of Adelaide, Australia, and an MSc and PhD at the Faculty of Medicine, University of Groningen, the Netherlands. Thereafter Yvonne worked for 12 years as clinical researcher within product development in the medical device industry specializing in the development and clinical application of innovative percutaneous interventional devices; imaging, innovative technology and clinical application are key words in her current position at the Radboud University Medical Centre, Nijmegen, The Netherlands.

After his medical degree, Leo Schultze Kool specialized in Radiology and in 1994 attained his PhD. From 1993-1997 he was head of angio-intervention at the University Medical Centre Leiden, and from 1997-2002 chairman of Radiology at the Antonius van Leeuwenhoek hospital in Amsterdam. He is currently head and professor of Interventional Radiology at the Radboud University Nijmegen Medical Centre, and leads research in image-based minimally invasive technology.

KlaasJan Renema studied technical Physics at the University of Groningen. After a PhD on MR spectroscopy he followed a traineeship for medical physicist. Currently he is working as Head Medical Physics of the dept. of Radiology at the University Medical Centre Nijmegen, the Netherlands.

Dr. Cornelis H. Slump is full professor at the University of Twente. In 1979 he graduated in Electrical Engineering at TU Delft and he has received the PhD degree in Theoretical Physics from Rijksuniversiteit Groningen in 1984. In 1983 he joined Philips Medical Systems and was group leader X-ray predevelopment cardiovascular. In 1989 he returned to academics as assistant professor at the University of Twente, Department of Electrical Engineering, Digital Signal Processing group. From 1994 – 1998 he was Dean of Education, in 1999 as full professor. His research interests are in functional medical imaging and image analysis.

References

Aurenhammer, F., Klein, R., Sack, J., Urrutia, J., 2000. Voronoi diagrams, in: Handbook of Computational Geometry. North-Holland, Amsterdam, pp. 201–290.

Beck, T., Biermann, C., Fritz, D., Dillmann, R., Pluim, J.P.W., Dawant, B.M., 2009. Robust model-based centerline extraction of vessels in CTA data, in: Proc. of SPIE, Lake Buena Vista, FL, USA. p. 72593O.

Bock, S., Kuhhnel, C., Boskamp, T., Peitgen, H., 2008. Robust vessel segmentation, in: Proc. of SPIE, San Diego, CA, USA. p. 691539.

Bruin, J.L.D., Baas, A.F., Buth, J., Prinssen, M., Verhoeven, E.L., Cuypers, P.W., van Sambeek, M.R., Balm, R., Grobbee, D.E., Blankensteijn, J.D., the DREAM Study Group, 2010. Long-Term outcome of open or endovascular repair of abdominal aortic aneurysm. N. Engl. J. Med. 362, 1881–1889.

Bunke, H., 1998. Error-Tolerant graph matching: A formal framework and algorithms, in: Proc. of the Joint IAPR International Workshops on Advances in Pattern Recognition, Springer-Verlag. pp. 1–14.

Cao, P., Rango, P.D., Parlani, G., Verzini, F., 2009. Durability of abdominal aortic endograft with the talent unidoc stent graft in common practice: Core lab reanalysis from the TAURIS multicenter study. J. Cardiovasc. Surg. 49, 859–865.

Cebral, J., Mut, F., Appanaboyina, S., Lohner, R., Miranda, C., Escrivano, E., Lylyk, P., Putman, C., Hu, X.P., Clough, A.V., 2009. Image-based analysis of blood flow modification in stented aneurysms, in: Proc. of SPIE, Lake Buena Vista, FL, USA. p. 72621G.

Cohen, L.D., Deschamps, T., 2007. Segmentation of 3D tubular objects with adaptive front propagation and minimal tree extraction for 3D medical imaging. Comput Methods Biomech Biomed Engin 10, 289.

Crum, W., Camara, O., Hill, D., 2006. Generalized overlap measures for evaluation and validation in medical image analysis. Medical Imaging, IEEE Transactions on 25, 1451–1461.

Demirci, S., Manstad-Hulaas, F., Navab, N., Miga, M.I., Wong, K.H., 2009. Quantification of abdominal aortic deformation after EVAR, in: Proc. of SPIE, Lake Buena Vista, FL, USA. p. 72611U.

Deschamps, T., Cohen, L.D., 2000. Fast extraction of minimal paths in 3D images and applications to virtual endoscopy. Med Image Anal 5, 281—299.

Desjardins, B., Kazerooni, E.A., 2004. ECG-Gated cardiac CT. AJR Am J Roentgenol 182, 993–1010.

Dijkstra, E., 1959. A note on two problems in connexion with graphs. Numerische Mathematik 1, 269—271.

Fahmi, R., Jerebko, A., Wolf, M., Farag, A.A., 2008. Robust segmentation of tubular structures in medical images, in: Proc. of SPIE, San Diego, CA, USA. p. 691443.

Fazel, R., Krumholz, H.M., Wang, Y., Ross, J.S., Chen, J., Ting, H.H., Shah, N.D., Nasir, K., Einstein, A.J., Nallamothu, B.K., 2009. Exposure to Low-Dose ionizing radiation from medical imaging procedures. New England Journal of Medicine 361, 849–857.

Frangi, A.F., Niessen, W.J., Vincken, K.L., Viergever, M.A., 1998. Multiscale vessel enhancement filtering. Lect Notes Comput Sci 1496, 130—137.

Freiman, M., Joskowicz, L., Sosna, J., Miga, M.I., Wong, K.H., 2009. A variational method for vessels segmentation: algorithm and application to liver vessels visualization, in: Proc. of SPIE, SPIE, Lake Buena Vista, FL, USA. p. 72610H.

Fuchs, T.O., Kachelriess, M., Kalender, W.A., 2000. System performance of multislice spiral computed tomography. IEEE Eng Med Biol Mag 19, 63—70.

Gülsün, M.A., Tek, H., 2008. Robust vessel tree modeling. Med Image Comput Comput Assist Interv 11, 602–611.

Hazer, D., Finol, E.A., Kostrzewa, M., Kopaigorenko, M., Richter, G., Dillmann, R., Hu, X.P., Clough, A.V., 2009. Computational biomechanics and experimental validation of vessel deformation based on 4D-CT imaging of the porcine aorta, in: Proc. of SPIE, Lake Buena Vista, FL, USA. p. 72621F.

Hernandez-Hoyos, M., Orkisz, M., Puech, P., Mansard-Desbleds, C., Douek, P., Magnin, I.E., 2002. Computer-assisted analysis of three-dimensional MR angiograms. Radiographics 22, 421—436.

van Herwaarden, J.A., Bartels, L.W., Muhs, B.E., Vincken, K.L., Lindeboom, M.Y., Teutelink, A., Moll, F.L., Verhagen, H.J., 2006. Dynamic magnetic resonance angiography of the aneurysm neck: Conformational changes during the cardiac cycle with possible consequences for endograft sizing and future design. J. Vasc. Surg. 44, 22—28.

Investigators, T.U.K.E.T., 2010. Endovascular versus open repair of abdominal aortic aneurysm. N. Engl. J. Med. 362, 1863–1871.

Jacobs, T.S., Won, J., Gravereaux, E.C., Faries, P.L., Morrissey, N., Teodorescu, V.J., Hollier, L.H., Marin, M.L., 2003. Mechanical failure of prosthetic human implants: A 10-year experience with aortic stent graft devices. J. Vasc. Surg. 37, 16–26.

Jandt, U., Schäfer, D., Grass, M., Rasche, V., 2009. Automatic generation of 3D coronary artery centerlines using rotational x-ray angiography. Med Image Anal 13, 846–858.

Kaftan, J.N., Tek, H., Aach, T., Pluim, J.P.W., Dawant, B.M., 2009. A two-stage approach for fully automatic segmentation of venous vascular structures in liver CT images, in: Proc. of SPIE, Lake Buena Vista, FL, USA. p. 725911.

Kirbas, C., Quek, F., 2004. A review of vessel extraction techniques and algorithms. ACM Comput. Surv. 36, 81–121.

Klein, A., Oostveen, L.J., Greuter, M.J.W., Hoogeveen, Y., Kool, L.J.S., Slump, C.H., Renema, W.K.J., 2009a. Detectability of motions in AAA with ECG-gated CTA: a quantitative study. Medical Physics 36, 4616–4624.

Klein, A., Renema, W.K., Kool, L.J.S., Slump, C.H., 2009b. Initial steps towards automatic segmentation of the wire frame of stent grafts in CT data, in: Proc. of IEEE-EMBS Benelux Chapter, Enschede, The Netherlands. pp. 116—119.

Klein, A., Renema, W.K., Oostveen, L.J., Kool, L.J.S., Slump, C.H., 2008. A segmentation method for stent-grafts in the abdominal aorta from ECG-gated CTA data, in: Proc. of SPIE, San Diego, CA, USA. p. 69160R.

Kleinstreuer, C., Li, Z., Farber, M.A., 2007. Fluid-Structure interaction analyses of stented abdominal aortic aneurysms. Annu Rev Biomed Eng 9, 169—204.

Langs, G., Paragios, N., Desgranges, P., Rahmouni, A., Kobeiter, H., 2011. Learning deformation and structure simultaneously: In situ endograft deformation analysis. Medical Image Analysis 15, 12–21.

Langs, G., Paragios, N., Donner, R., Desgranges, P., Rahmouni, A., Kobeiter, H., 2007. Motion analysis of endovascular Stent-Grafts by MDL based registration, in: Proc IEEE Int Conf Comput Vis, pp. 1–8.

Lee, J., Beighley, P., Ritman, E., Smith, N., 2007. Automatic segmentation of 3D micro-CT coronary vascular images. Med Image Anal 11, 630—647.

Lesage, D., Angelini, E.D., Bloch, I., Funka-Lea, G., 2009. A review of 3D vessel lumen segmentation techniques: Models, features and extraction schemes. Med Image Anal 13, 819–845.

Li, Z., Kleinstreuer, C., 2006a. Analysis of biomechanical factors affecting stent-graft migration in an abdominal aortic aneurysm model. J Biomech 39, 2264—2273.

Li, Z., Kleinstreuer, C., 2006b. Computational analysis of type II endoleaks in a stented abdominal aortic aneurysm model. J Biomech 39, 2573–2582.

Lu, J., Egger, J., Wimmer, A., Grosskopf, S., Freisleben, B., Miga, M.I., Cleary, K.R., 2008. Detection and visualization of endoleaks in CT data for monitoring of thoracic and abdominal aortic aneurysm stents, in: Proc. of SPIE, SPIE, San Diego, CA, USA. p. 69181F.

Manduca, A., Fletcher, J.G., Wentz, R.J., Shields, R.C., Vrtiska, T.J., Siddiki, H., Nielson, T., Hu, X.P., Clough, A.V., 2009. Reproducibility of aortic pulsatility measurements from ECG-gated abdominal CTA in patients with abdominal aortic aneurysms, in: Proc. of SPIE, SPIE, Lake Buena Vista, FL, USA. p. 72620L.

Mattes, J., Steingruber, I., Netzer, M., Fritscher, K., Kopf, H., Jaschke, W., Schubert, R., 2005. Spatio-temporal changes and migration of stent grafts after endovascular aortic aneurysm repair. Int. Congr. Ser. 1281, 393–397.

Muhs, B.E., Vincken, K.L., van Prehn, J., Stone, M.K., Bartels, L.W., Prokop, M., Moll, F.L., Verhagen, H.J., 2006. Dynamic Cine-CT angiography for the evaluation of the thoracic aorta; insight in dynamic changes with implications for thoracic endograft treatment. Eur J Vasc Endovasc Surg 32, 532—536.

Prokop, M., 2005. New challenges in MDCT. European Journal of Radiology 15, 35—45.

Quek, F., Kirbas, C., 2001. Vessel extraction in medical images by wave-propagation and traceback. IEEE Trans Med Imaging 20, 117–131.

Roos, J.E., Hellinger, J.C., Hallet, R., Fleischmann, D., Zarins, C.K., Rubin, G.D., 2005. Detection of endograft fractures with multidetector row computed tomography. J. Vasc. Surg. 42, 1002–1006.

Seljebotn, D.S., 2009. Fast numerical computations with cython, Proc. of the 8th Python in Science Conference, Pasadena, CA USA. pp. 15—22.

Stavropoulos, S.W., Charagundla, S.R., 2007. Imaging techniques for detection and management of endoleaks after endovascular aortic aneurysm repair. Radiology 243, 641—655.

Swillens, A., Lanoye, L., Backer, J.D., Stergiopulos, N., Verdonck, P.R., Vermassen, F., Segers, P., 2008. Effect of an abdominal aortic aneurysm on wave reflection in the aorta. IEEE Trans Biomed Eng 55, 1602—1612.

Teutelink, A., Muhs, B., Vincken, K.L., Wartels, L.W., Cornelissen, S.A., van Herwaarden, J.A., Prokop, M., Moll, F.L., Verhagen, H.J.M., 2007. Use of dynamic computed tomography to evaluate pre- and postoperative aortic changes in AAA patients undergoing eneurysm repair. J. Endovasc. Ther. 14, 44–49.

Wentz, R., Manduca, A., Fletcher, J.G., Siddiki, H., Shields, R.C., Vrtiska, T., Spencer, G., Primak, A.N., Zhang, J., Nielson, T., McCollough, C., Yu, L., 2007. Automatic segmentation and co-registration of gated CT angiography datasets: measuring abdominal aortic pulsatility, in: Proc. of SPIE, San Diego, CA, USA. p. 65111I.

Wink, O., Niessen, W., Viergever, M., 2004. Multiscale vessel tracking. IEEE Trans Med Imaging 23, 130–133.

Worz, S., Godinez, W.J., Rohr, K., Pluim, J.P.W., Dawant, B.M., 2009. Segmentation of 3D tubular structures based on 3D intensity models and particle filter tracking, in: Proc. of SPIE, Lake Buena Vista, FL, USA. p. 72591P.

Zarins, C.K., White, R.A., Schwarten, D., Kinney, E., Diethrich, E.B., Hodgson, K.J., Fogarty, T.J., 1999. AneuRx stent graft versus open surgical repair of abdominal aortic aneurysms: multicenter prospective clinical trial. J. Vasc. Surg. 29, 292–305.

Zhou, C., Chan, H., Chughtai, A., Patel, S., Agarwal, P., Hadjiiski, L.M., Sahiner, B., Wei, J., Ge, J., Kazerooni, E.A., Giger, M.L., Karssemeijer, N., 2008. Automated segmentation and tracking of coronary arteries in ECG-gated cardiac CT scans, in: Proc. of SPIE, San Diego, CA, USA. p. 69150O.